New Measurement of the Vertical Atmospheric Density Profile from Occultations of the Crab Nebula with X-Ray Astronomy Satellites Suzaku and Hitomi

Satoru Katsuda[1], Hitoshi Fujiwara[2], Yoshitaka Ishisaki[3,4], Yoshitomo Maeda[4], Koji Mori[5,4], Yuko Motizuki[6], Kosuke Sato[1], Makoto S. Tashiro[4,1], and Yukikatsu Terada[1,4]

[1]Graduate School of Science and Engineering, Saitama University, 255 Shimo-Ohkubo, Sakura, Saitama 338-8570, Japan
[2]Faculty of Science and Technology, Seikei University, Tokyo, Japan
[3]Department of Physics, Tokyo Metropolitan University, 1-1 Minami-Osawa, Hachioji, Tokyo 192-0397, Japan
[4]Institute of Space and Astronautical Science (ISAS), Japan Aerospace Exploration Agency (JAXA), 3-1-1 Yoshinodai, Chuo-ku, Sagamihara, Kanagawa, 252-5210, Japan
[5]Department of Applied Physics and Electronic Engineering, University of Miyazaki, 1-1, Gakuen Kibanadai-nishi, Miyazaki 889-2192, Japan
[6]RIKEN Nishina Center, Hirosawa 2-1, Wako 351-0198, Japan

Key Points:

- Combined O and N densities at altitudes 70–220 km are measured from Earth occultations of the Crab nebula using X-ray astronomy satellites, Suzaku and Hitomi.
- The vertical density profile is in general agreement with a predicted profile from the NRLMSISE-00 model, except for altitudes 80–110 km in which the density is significantly smaller than the prediction by the NRL model.
- This density deficit could be due to either long-term radiative cooling of the upper atmosphere or imperfect modeling.

Corresponding author: Satoru Katsuda, katsuda@phy.saitama-u.ac.jp

Abstract

We present new measurements of the vertical density profile of the Earth's atmosphere at altitudes between 70 and 220 km, based on Earth occultations of the Crab nebula observed with the X-ray Imaging Spectrometer onboard Suzaku and the Hard X-ray Imager onboard Hitomi. X-ray spectral variation due to the atmospheric absorption is used to derive tangential column densities of the absorbing species, i.e., N and O including atoms and molecules, along the line of sight. The tangential column densities are then inverted to obtain the atmospheric number density. The data from 221 occultation scans at low latitudes in both hemispheres from September 15, 2005 to March 26, 2016 are analyzed to generate a single, highly-averaged (in both space and time) vertical density profile. The density profile is in good agreement with the NRLMSISE-00 model, except for the altitude range of 80–110 km, where the measured density is $\sim$30% smaller than the model. Such a deviation is consistent with the recent measurement with the SABER aboard the TIMED satellite (Cheng et al., 2020). Given that the NRLMSISE-00 model was constructed some time ago, the density decline could be due to the radiative cooling/contracting of the upper atmosphere as a result of greenhouse warming in the troposphere. However, we cannot rule out a possibility that the NRL model is simply imperfect in this region. We also present future prospects for the upcoming Japan-US X-ray astronomy satellite, XRISM, which will allow us to measure atmospheric composition with unprecedented spectral resolution of $\Delta E \sim 5\,\mathrm{eV}$ in 0.3–12 keV.

1 Introduction

The neutral density in the lower thermosphere, defined as an altitude range of 70–220 km in this paper, is essential to estimate the global meteoric mass input and to derive the momentum flux from tropospheric gravity waves. Also, the lower thermosphere is thought to be sensitive to the climate change due to greenhouse gases; global cooling would occur in the upper atmosphere in conjunction with global warming in the troposphere due to long-term increase of greenhouse gas concentrations, which was first pointed out by Roble and Dickinson (1989). The cooling should cause the atmosphere to contract, leading to a density decrease at a fixed altitude.

However, measurements of neutral densities in the lower thermosphere are still scarce. Neutral densities are largely measured by means of in-situ instruments onboard sounding rockets (80–100 km) and satellites ($\sim$400 km), and thus the 100–300 km altitude is left as the "thermospheric gap" (Oberheide et al., 2011). Although there are some early density measurements based on occultations of the Sun in ultraviolet wavelengths (e.g., Norton & Warnock, 1968; Hays et al., 1972; Ackerman et al., 1974; Meier et al., 1992; Aikin et al., 1993), these studies mainly focused on molecular oxygen which is a minor species in the lower thermosphere, leaving large uncertainties on the total mass density. So far, there are very limited remote-sensing measurements to fill this gap (e.g., Meier et al., 2015).

Atmospheric occultations of X-ray astronomical sources offer a unique opportunity to measure the neutral density in the lower thermosphere. This technique was first demonstrated/published by Determan et al. (2007) who analyzed data during atmospheric occultations of the Crab nebula and Cygnus X-2 using ARGOS/USA and RXTE/PCA. We note that there is an interesting earlier X-ray measurement of the atmospheric thickness of Titan (i.e., the Saturn's largest satellite), when it transited the Crab nebula on 2003-01-05 (Mori et al., 2004). The advantage of the X-ray occultation method is that it is independent of the chemical, ionization, and excitation processes, because X-rays are directly absorbed by inner K-shell and L-shell electrons, so that X-rays see only atoms (within molecules). In other words, the X-ray occultation method cannot distinguish between atoms and molecules, but allows us to measure the total neutral density without the complexity involved with modeling absorption processes.

By analyzing occultations of the Crab nebula taken in November 2005, Determan et al. (2007) reported that 50% and 15% smaller densities at altitudes 100–120 km and 70–90 km, respectively, than the empirical density model, i.e., the Naval-Research-Laboratory's-Mass-Spectrometer-Incoherent-Scatter-Radar-Extended model (NRLMSISE-00: Picone et al., 2002). As discussed in Wood and Ray (2017), this deviation is qualitatively consistent with the density decrease due to greenhouse cooling in the upper atmosphere, given that a few decades have past after the NRL model was constructed. However, it is important to cross-check from other observations, and to distinguish between greenhouse gases and solar effects by monitoring over times longer than the solar cycle. Therefore, more observations are required to firmly conclude (or exclude) this interpretation.

Here, we present a new density measurement in the lower thermosphere region, based on occultations of the Crab nebula observed with the Japanese X-ray astronomy satellites Suzaku (Mitsuda et al., 2007) and Hitomi (Takahashi et al., 2018). The combination of the X-ray Imaging Spectrometer (XIS, sensitive in 0.5–12 keV: Koyama et al. (2007)) and the Hard X-ray Imager (HXI, sensitive in 5–80 keV: Nakazawa et al. (2018)) aboard Suzaku and Hitomi, respectively, allows us to investigate the density structure in a range of altitude between 70 km and 220 km. The paper is organized as follows. Section 2 describes occultation data of the Crab nebula acquired with Suzaku and Hitomi. Section 3 describes analysis of the data, and shows the retrieved vertical density distribution. Section 4 discusses the results, and provides future prospects. Section 5 gives conclusions of this paper.

2 Observations

We analyze data during Earth occultations of the Crab nebula, obtained with the X-ray astronomy satellites Suzaku and Hitomi. The Crab nebula and the Crab pulsar were created in a supernova explosion observed in 1054 AD. Various X-ray satellites have used the Crab as a standard candle to perform their calibrations in the past, because it is one of the brightest sources in the X-ray sky, and its intensity is nearly constant and the spectral shape is a simple, featureless power-law.

Both Suzaku and Hitomi carried multiple instruments with different capabilities. Of these, we focus on Suzaku/XIS and Hitomi/HXI, because they are complementary in terms of the energy coverage; the XIS and HXI cover 0.2–12 keV and HXI in 5–80 keV, respectively, and also they have time and spatial resolutions sufficient for our purpose.

As illustrated in the upper panel of Figure 1, X-ray sources appear to set and rise behind the Earth every orbit. This is because the two X-ray astronomy satellites are in low Earth orbits, i.e., $\sim$560 km (Suzaku) and $\sim$575 km (Hitomi), and also the attitude of the satellites is 3D fixed during each observation. The lower panel of Figure 1 demonstrates how the X-ray spectrum changes during an atmospheric occultation of the Crab nebula, where the spectra are the sums of all the data listed in Table 1. The data in ELV 10°–15° are free from the atmospheric attenuation, where ELV is defined as the telescope's, i.e., Crab's elevation angle measured from the Earth limb (see also Figure 1). As the occultation progresses (decreasing ELV or tangential height), the X-ray intensity gradually decreases from the low-energy band.

In principle, all X-ray sources can be our targets, but in practice, the targets are very limited for the following reasons. First, the targets must be very bright, given that typical occultations take only $\sim$30 s, which needs to be further divided into shorter time bins to obtain a vertical density distribution. Second, the target's spectrum and intensity should be constant during the occultation to avoid confusion between intrinsic source variations and atmospheric absorption. Third, the targets are preferably point sources for simplicity of the analysis.

The source brightness also has an important impact on the time resolution of Suzaku/XIS. The large angular velocity of the telescope, $0.06^\circ\,s^{-1}$, for both satellites, as well as the short transition period from unattenuation to full attenuation, $\sim$30 s, require time resolution of the order of second or less to resolve vertical atmospheric density structures. The time resolution of the XIS in a normal mode is 8 s. This corresponds to $\sim 0.5^\circ$ ($\sim 0.06^\circ\,s^{-1} \times 8\,s$) or $\sim$20 km at the altitude of 100 km, and is too coarse for our diagnostic purposes. Therefore, we decided to focus on data taken in a special mode, i.e., 0.1-s burst mode, in which the exposure time is limited to 0.1 s for each 8-s sampling. This mode was prepared to avoid pile-up effects occurring for super-bright sources (Yamada et al., 2012, for more details). As for Hitomi/HXI, the time resolution does not matter, because the time-tagging system for the HXI is event-by-event with excellent resolution of 25.6 μs.

The Crab nebula is an unrivaled source to meet all the criteria above. Also, it was usually observed with the XIS in the 0.1-s burst mode, and thus is an ideal source for the measurement of the atmospheric density profile. In addition, there are numerous Suzaku data for the Crab nebula, because it was one of important calibration sources for Suzaku, as is usual for X-ray astronomy satellites. This is another advantage with the Crab nebula. Although the Crab nebula is not a point source, its angular size of $R \sim 1'$ is smaller than the half-power diameter (HPD) of the X-ray telescopes on Suzaku (HPD$\sim 2'$: Serlemitsos et al., 2007) and Hitomi (HPD$\sim 1.7'$: Matsumoto et al., 2018). Therefore, it can be considered nearly a point source for both satellites.

Table 1 summarizes basic information about all occultations of the Crab nebula analyzed in this paper. The third column describes the time for each occultation, from ELV = 5° (0°) to ELV = 0° (5°) for each setting (rising). The fourth column indicates the Earth's latitude and longitude at the tangent point, defined as the altitude of the closest approach to the Earth surface along the telescope line of sight. We note that most observations are taken in the latitude from -20° to $+40^\circ$. This is because the inclination angles of both satellites are 31°, and the telescope is 22° inclined to the north, toward the Crab nebula. Also, ΔELV1 in the fifth column is an ELV angle required to correct for the ELV offset caused in the process of ELV calculation. The Earth radius was assumed to be the equatorial radius of 6378.137 km in the ELV calculation. But in reality, the Earth radius decreases with increasing latitudes (e.g., Equation 6 in Aikin et al., 1982). Therefore, ELV values are underestimated at higher latitudes by an amount of ΔELV1, which is the offset to be added to derive true ELV values. ΔELV2 in the sixth column will be described in the next section.

Suzaku observed the Crab nebula almost every spring and autumn for ten years. Many of these observations captured Crab at off-axis positions for calibration purposes. For simplicity of our analysis, we selected observations aiming at the Crab nebula at on-axis positions. However, we allow tolerance of $\sim 3'$ offset in Decl. (north-south) direction. This is because the Crab nebula sets and rises roughly from the east-west (i.e., R.A.) direction, and thus the north-south offset does not affect setting and rising times by much. We also discarded short-exposure (duration less than 10 ks) observations for Suzaku to improve the efficiency of our analysis.

3 Analysis and Results

When X-ray sources set into (or rise from) the Earth's atmosphere, we see rounded, not sharp-edged, intensity profiles. The upper panel of Figure 2 demonstrates such occultation light curves as a function of ELV, where the data are taken from Obs.ID 106014010, i.e., occultation # from 106 to 134 in Table 1. The gradual increase/decrease of the X-ray intensity against ELV clearly shows the effect of atmospheric absorption. We note that this profile is corrected for ΔELV1, as mentioned in the previous section.

Obviously, the two (set and rise) groups are shifted with each other along the ELV axis. If we attributed the ELV shift of $0.45°$ to the difference of the atmospheric densities, then the density difference between the set and rise would be more than an order of magnitude. Although the setting and rising are taking place in spring in the northern hemisphere and autumn in the southern hemisphere, respectively (see Table 1), seasonal variations are expected to be much smaller in the NRLMSISE-00 model, which is supported by recent observations (Cheng et al., 2020). There are no other natural explanations for such a large density variation. Therefore, we suspect that the ELV shift is caused by systematic uncertainties on ELV and/or its time assignments. It should be noted that the ELV shift for Hitomi/HXI is basically smaller than that for Suzaku/XIS. Therefore, the following correction method is particularly important for Suzaku, although we also applied it for Hitomi to take account possible systematic uncertainties.

Assuming that the set and rise profiles are ideally identical, we artificially shift the ELV values, such that the set and rise profiles converge with each other. Among some possibilities to shift ELV, one fair method would be to shift ELV values for set and rise by an equal amount in the opposite direction. A strength of this correction method is that such an opposite ELV shift can be naturally achieved by shifting the time for ELV, as demonstrated in Figure 2. As for the example case in Figure 2, the amount of ELV shift (ΔELV2) is $\pm 0.226°$. This can be obtained by shifting the ELV time by 3.6 s. This time shift could be due to either the time-assignment error or the uncertainty of the satellite position, or both of them. A time shift of 1 s is equivalent to a position shift of 7.5 km for a satellite's orbital velocity of $7.5\,\mathrm{km\,s^{-1}}$ as expected for both Suzaku and Hitomi. Thus, the time shift of 3.6 s could be due to a misplacement of the satellite by 27 km ($= 7.5\,\mathrm{km\,s^{-1}} \times 3.6\,\mathrm{s}$). Such a large position error may be expected for the Suzaku satellite, given that there is a possibility that the epoch of the coordinate system used to determine the orbital elements was incorrectly taken between "J2000" and "True of Date". Position erros caused by the possible incorrect epoch are quantitatively estimated for a few cases to range from $\sim$9 km to $\sim$20 km. This can explain two thirds of the discrepancy. The remaining systematic error of the order of 10 km would reflect uncertainties on the orbit determination.

Identifying sources of the systematic error is beyond the scope of this paper. Instead, we simply shift ELV by $\pm\Delta$ELV2, such that set and rise profiles are matched with each other. Specifically, we calculated ΔELV2 from $\mathrm{ELV}_{1/2}$(rise)$-\mathrm{ELV}_{1/2}$(set), where $\mathrm{ELV}_{1/2}$ is defined as the elevation angle at which the X-ray intensity becomes half of the unattenuated level. We measured $\mathrm{ELV}_{1/2}$ by fitting the occultation light curves with a phenomenological model consisting of Gaussian plus constant components. Thus-derived ΔELV2 values are listed in the right-end column of Table 1. We can see that ΔELV2 ranges from $\pm 0.04°$ to $\pm 0.23°$, and the variation is unpredictable. The random variation also supports the idea that the ELV shifts between set and rise profiles are not real.

Figures 3 and 4 exhibit all the ELV-corrected (both ΔELV1 and ΔELV2) occultation profiles taken with Suzaku and Hitomi, respectively. The intensity is normalized at the unattenuated level for each Obs.ID. We fit these profiles with the same phenomenological model as described in the previous paragraph, and show the best-fit models as black curves in Figures 3 and 4. We also give $\mathrm{ELV}_{1/2}$ values in the left upper corner in each panel. The $\mathrm{ELV}_{1/2}$ value for Hitomi is smaller than that of Suzaku. This is because Hitomi/HXI is sensitive to the higher energy band than Suzaku/XIS is. Within Suzaku data, there is another remarkable variation for $\mathrm{ELV}_{1/2}$, ranging from $2.43°$ to $2.54°$. This is probably due to remaining systematic uncertainties on ELV and/or real density variation in the upper atmosphere.

Next, we analyzed ELV-separated X-ray spectra to derive atmospheric column densities at various tangential altitudes. It would be best if we can examine X-ray spectra for every single occultation. However, photon statistics and sampling rates in one occultation scan are so limited (especially for Suzaku) that we decided to accumulate all occultations in each Obs.ID. We further combine short-exposure observations, i.e., Obs.IDs 100023010, 100023020, and 101011060, to improve the effective sampling rate. The ELV bins for our spectral analysis are optimized to be 0.1°, 0.3°, and 0.6° in ELV ranges of 1.5°–3.5°, 3.5°–4.7°, and 4.7°–5.3°, respectively. To improve the photon statistics, we combine data from Suzaku's XIS0, XIS1, and XIS3, and Hitomi's HXI1 and HXI2. For Suzaku/XIS, we exclude a central circular region with a radius of 40″ where pileup fraction exceeds 3% (Yamada et al., 2012).

Figures 5 and 6 exhibit example X-ray spectra from Suzaku/XIS (Obs.ID 106012010) and Hitomi/HXI, respectively. Clearly, the X-ray intensity decreases from the low-energy band as the line-of-sight goes deeper into the atmosphere. We fit these spectra with an absorbed, power-law model, using the XSPEC package (Arnaud, 1996). The absorption model consists of two components: one for the interstellar absorption (the `TBabs`: Wilms et al. (2000)) and the other for the atmospheric absorption (the `vphabs` with the photoionization cross-sections by Verner et al. (1996)). As described in Determan et al. (2007), the accuracy of absolute cross sections is knwon to be better than 5%, which is smaller than a typical statistical uncertainty on each measurement (cf., Tables 2 and 3). We first determine an unattenuated spectral shape for each observation, by fitting an X-ray spectrum taken during ELV=10°–15° without the atmospheric absorption. The spectral-fit parameters for the Crab nebula in all epochs are in reasonable agreement with previous measurements (Hagino et al., 2018).

Then, we fit ELV-binned X-ray spectra with the model that takes account of the atmospheric absorption. In this fitting procedure, all parameters related to the Crab nebula, i.e., the hydrogen column density for the interstellar absorption, the photon index and normalization of the power-law component, are fixed at the best-fit values obtained for each Obs.ID. In the atmospheric absorption component, we consider N, O, and Ar, with other elements fixed to zero. We fix relative abundances of O/N and Ar/N to those expected in the NRLMSISE-00 model at each altitude of interest (Picone et al., 2002), because our data do not allow us to measure individual contributions of the three elements. As shown in Figures 5 and 6, this model fits the data fairly well. Below, we provide the summed density of N and O, because both of them are sensitive to the X-ray absorption in the thermosphere. According to the NRLMSISE-00 model, the density of Ar is expected to be much smaller (less than 1%) than the N+O density in the lower thermosphere. Therefore, we do not include Ar in the following discussion.

Tables 2 and 3 show the N+O column densities at all ELV bins for Suzaku/XIS and Hitomi/HXI, respectively. The two data sets for Suzaku, i.e., Obs.IDs 106012010 and 106014010 which were taken half-year apart, represent extreme $ELV_{1/2}$ cases (see Figure 3). As expected, there is a substantial difference in the atmospheric column densities by a factor of 2 between the two. At this moment, it is unclear if this change is real or not, but we suspect that this is caused by a systematic uncertainty on ELV. This is because two adjacent observations with similar tangent latitudes, 100023010 and 200023020, for which densities are expected to agree with each other, show a relatively large $ELV_{1/2}$ difference of 0.06°. In addition, the $ELV_{1/2}$ variation seems random, not showing systematic long-term trends nor seasonal dependence. A possible source of systematic errors on $ELV_{1/2}$ is an uncertainty of the satellite position in the vertical direction, which should result in the same ELV offsets for both set and rise profiles, and thus can not be taken into account by the ELV correction applied above. At this moment, it is difficult to reveal the source of ELV errors. Therefore, we here compute an average of the ten Suzaku data, which hopefully mitigate the uncertainty on ELV. We also take standard deviations of the ten Suzaku data sets as our conservative measurement errors; the standard deviations are generally a few times larger than the statistical uncertainties on each data point for a single Obs.ID. The results are listed in the right-end column of Table 2.

Figure 7 compares our measured N+O column densities with those expected by the NRLMSISE-00 model at three different dates: 1) 2009-03-14 for the solar minimum, 2)

2012-03-14 for the solar maximum, when Obs.ID 106014010 data were taken, 3) 2016-03-26 for the intermediate phase, when Obs.ID 100044010 data were taken. The model curves are calculated at a location (latitude, longitude) = (0°, 0°) and times from 0:00 to 23:00 (UT) by a step of an hour to take account of the local time dependence. In fact, the models at three epochs agree with each other below 150 km altitude. This is reasonable because the region below 150 km altitude is almost independent on the solar cycle (e.g., Meier et al., 2015). Our measurements are in general agreement with the model.

We note in Figure 7 that errors below ∼100 km altitude are systematically smaller than those in the upper altitudes. This is because errors on the five data points from the bottom represent statistical uncertainties for the single Hitomi/HXI observation, whereas those on other data points represent standard deviations for ten Suzaku/XIS observations. Without averaging, the Hitomi/HXI data could be biased. However, fortunately, we expect that the ELV accuracy for Hitomi is significantly improved from Suzaku, because the possible major error source on ELV, i.e., the wrong coordinate system, suspected for Suzaku was resolved for Hitomi. Nonetheless, we introduced $\pm\Delta$ELV2 of ∼0.069° to match the set and rise profiles for Hitomi (see Figure 4). This is relatively small compared with those for Suzaku, but the presence of ELV shift indicates unresolved systematic errors on ELV even for Hitomi.

We invert the tangential column number density to the local number density at the tangent point, using the technique developed by Roble and Hays (1972). Specifically, we followed their technique to stabilize the small random errors in the data, by using the exponential form to approximate the atmospheric column density distribution. In this procedure, we first need to obtain the normalization and decay constant of the exponential function at each data point. To this end, the data point of our interest and its surrounding two data points in both sides are fitted with an exponential function. Then, the best-fit parameters for the exponential function are used to derive the local density, by using Equation (9) in Roble and Hays (1972). The errors are propagated according to the equation in the appendix of Roble and Hays (1972). As a result, we obtain a vertical density distribution in Figure 8. We also plot a prediction by NRLMSISE-00 on 2016-03-26 when the Hitomi/HXI data were obtained. As expected from Figure 7, the density profile is in general agreement with the NRLMSISE-00 model. However, we can see a significant density deficit at altitudes around 100 km, which is magnified in the inset of Figure 8.

4 Discussion

We have measured the atmospheric N+O density in the altitude range of 70–220 km and the latitude of −20°–40° during a period from 2005 to 2016, with the X-ray astronomy satellites Suzaku and Hitomi. We analyzed data from 221 occultation scans in total. To minimize the possible systematic uncertainty on ELV, we constructed a single, averaged vertical density profile as shown in Figure 8. For comparison, Figure 8 also shows recent measurements that overlaps the altitude range of our interest (Determan et al., 2007; Meier et al., 2015; Thiemann et al., 2017; Cheng et al., 2020). We here focused on literature that lists N and O densities, excluding measurements of the O_2 density (e.g., Lumpe et al., 2007), as O_2 is a minor species in the thermosphere. When plotting the literature data in Figure 8, we converted the data (either N_2+O or total mass density) into the total number densities of N and O, assuming the altitude-dependent atmospheric composition in the NRLMSISE-00 model.

Our data are consistent with results from TIMED/SABER's infrared (IR) observations at 72 km and 100 km (Cheng et al., 2020), as well as RXTE/PCA's X-ray occultation observations at altitudes 73–93 km (Determan et al., 2007). Our data are significantly larger than the RXTE/PCA measurements in altitudes 100–120 km. It should be noted, however, that Determan et al. (2007) also presented ∼1.7 times larger densities in the 70–150 km range from both RXTE/PCA and ARGOS/USA, based on their analysis using lower-energy emission (3–19 keV and 2–12 keV for PCA and USA, respectively, hence sensitive to higher altitudes) and a model with a single-density scalar at all altitudes. This result is consistent with our measurement, and in fact better connects to the density in the lower altitude (Determan et al., 2007). Therefore, we suspect that the deviation seen at altitudes 100–120 km is controversial. Above 120 km, our data generally agree with two previous measurements by TIMED/GUVI (Meier et al., 2015, data taken on day 77 in 2002) and PROBA2/LYRA (Thiemann et al., 2017). However, the data taken on day 194 in 2006 (Meier et al., 2015) show a significantly lower density than ours. This might be partly due to the latitude dependence on the atomic O density, which decreases more rapidly with increasing height at higher latitudes. We conclude that our data are in reasonable agreement with earlier density measurements.

To compare our measurement and the model more quantitatively, we compare in Figure 9 the data with a time-averaged density model on 2016-03-26, when Hitomi/HXI data were taken. The right-hand panel shows the data-to-model ratio as a function of altitude. As mentioned in the previous section, the measured density profile is in good agreement with the NRLMSISE-00 model, except for the altitude range of 80–110 km, where the data are significantly smaller than the model with a maximum deficit of -30% at altitude of $\sim$95 km.

Both theoretical models and observations have suggested that the increasing greenhouse gas (e.g., CO_2 and CH_4) concentration in the troposphere causes the upper atmosphere to cool and contract, resulting in a corresponding density decrease at a given height (e.g., Roble & Dickinson, 1989; Keating et al., 2000). In the troposphere, CO_2 is optically thick and traps IR radiation emitted by the Earth's surface. In the stratosphere and above, CO_2 is optically thin and emits infrared radiation to space, which cools and contracts these regions. Emmert (2015) summarized long-term density trends from both modeling studies and observations. Although there is a significant scatter among the data, the trend is all negative (decreasing density) in the thermosphere. It is interesting to note that Akmaev et al. (2006) predicted that a layer near 110 km shows a maximum density reduction of -6.5% per decade, which was later quantitatively confirmed by radar observations of meteor trails (Stober et al., 2014). The ratio between our data and the NRLMSISE-00 model in Figure 9 shows a maximum of the density decline at $\sim$100 km altitude, which is qualitatively consistent with the trend found by Akmaev et al. (2006).

We do not see a significant long-term density variation within our data. Although $ELV_{1/2}$ values for occultation light curves indicate significant density variations from observation to observation, we consider that this variation is more likely caused by a systematic uncertainty on ELV, as we described in the previous section. There is no clear density difference compared with past observations, either. In order to discuss temporal variations of the atmospheric density, it is critical to reveal the possible systematic uncertainty on the ELV parameter, and refine the ELV values. This is left for our future work.

Occultations of X-ray astronomical sources have been detected with other X-ray astronomy satellites in low Earth orbits, including terminated ones such as Ginga (Makino & ASTRO-C Team, 1987) and ASCA (Tanaka et al., 1994), as well as in-operation ones such as NuSTAR (Harrison et al., 2013) and NICER (Gendreau et al., 2016). Analyses of the data from these satellites will allow us to investigate a long-term trend of the atmospheric density. Specifically, NuSTAR is suitable to diagnose the density deficit region at the altitude $\sim$100 km, thanks to its good sensitivity in a wide energy range of 3–80 keV. NICER has an unprecedented throughput that will allow us to obtain the density profile every single occultation. Also, the X-Ray Imaging and Spectroscopy Mission (XRISM: Tashiro et al., 2018), the Japan-US X-ray astronomy mission scheduled to be launched in 2022, will carry an X-ray micro-calorimeter (Resolve: Ishisaki et al., 2018) that will allow for high-resolution spectroscopy of a resolution of $\Delta E \sim 5$ keV with little energy dependence in 0.2–12 keV. To demonstrate its capability, we simulate XRISM/Resolve spectra expected during the occultation of the Crab nebula, as shown in Figure 10 left and right for ELV 3.5°–3.8° and 2.1°–2.2°, respectively. Absorption edges of N at 0.41 keV and O at 0.54 keV can be seen at higher tangential altitudes, and that of Ar at 3.2 keV can be seen at lower tangential altitudes. The depths of these edges will tell us the composition of the atmosphere. These simulations are performed for an exposure time of 500 s. This exposure time will be accumulated by ∼100 and ∼300 occultations for ELV 3.5°–3.8° and 2.1°–2.2°, respectively. Therefore, it will take a few years for us to take the spectrum of this quality from calibration data alone, but it is certainly doable with XRISM/Resolve.

Finally, we point out that measuring atmospheric densities with X-ray astronomy satellites has just started, and thus more experiences are essential to obtain deeper insights into unresolved issues such as the source of systematic uncertainties on ELV.

5 Conclusions

By analyzing data during atmospheric occultations of the Crab nebula, obtained with two X-ray astronomy satellites Suzaku and Hitomi, we measured a vertical density profile of the Earth's atmosphere in altitudes of 70–220 km. We provided one density profile, by averaging 221 occultations taken during 2005–2016. The vertical density profile is generally consistent with a prediction by the empirical NRLMSISE-00 model. Our measurement is also generally consistent with several earlier measurements (Determan et al., 2007; Meier et al., 2015; Thiemann et al., 2017; Cheng et al., 2020). We found a significant density deficit at the altitude range of 80–110 km. The strong density deficit at ∼100 km altitude is qualitatively consistent with a model prediction and observation that claims long-term cooling in the upper atmosphere due to IR radiation from increasing greenhouse gases (Akmaev et al., 2006; Stober et al., 2014). It is important to monitor the atmospheric density to clarify if the possible long-term trend is true or not. This work can be done by analyses of data acquired with past, in-operation, and future X-ray astronomy satellites. In addition, with the upcoming XRISM, we will be able to measure the composition of the upper atmosphere from K-shell absorption edges of N, O, and Ar.

Acknowledgments

All the data used in this paper can be found at NASA's HEASARC website, https://heasarc.gsfc.nasa.gov. We are grateful to all the members of Suzaku and Hitomi teams. We thank Ms. Mina Ogawa for providing us with information about possible Suzaku's position uncertainty. This work was supported by the Japan Society for the Promotion of Science KAKENHI grant numbers 20K20935 (SK and MST), 16H03983 (KM). This work was partly supported by Leading Initiative for Excellent Young Researchers, MEXT, Japan.

References

Ackerman, M., Simon, P., von Zahn, U., & Laux, U. (1974, November). Simultaneous upper air composition measurements by means of UV monochromators and mass spectrometers. *Journal of Geophysical Research*, *79*(31), 4757. doi: 10.1029/JA079i031p04757

Aikin, A. C., Hedin, A. E., Kendig, D. J., & Drake, S. (1993, October). Thermospheric molecular oxygen measurements using the ultraviolet spectrometer on the Solar Maximum Mission spacecraft. *Journal of Geophysical Research*, *98*(A10), 17607-17614. doi: 10.1029/93JA01468

Aikin, A. C., Woodgate, B., & Smith, H. J. P. (1982, July). Atmospheric ozone determination by solar occultation using the UV spectrometer on the Solor Maximum Mission. *Applied Optics*, *21*(13), 2421-2424. doi: 10.1364/AO.21.002421

Akmaev, R. A., Fomichev, V. I., & Zhu, X. (2006, December). Impact of middle-atmospheric composition changes on greenhouse cooling in the upper atmosphere. *Journal of Atmospheric and Solar-Terrestrial Physics*, *68*(17), 1879-1889. doi: 10.1016/j.jastp.2006.03.008

Arnaud, K. A. (1996, January). XSPEC: The First Ten Years. In G. H. Jacoby & J. Barnes (Eds.), *Astronomical data analysis software and systems v* (Vol. 101, p. 17).

Cheng, X., Yang, J., Xiao, C., & Hu, X. (2020, March). Density Correction of NRLMSISE-00 in the Middle Atmosphere (20100 km) based on TIMED/SABER Density Data. *Atmosphere*, *11*(4), 341. doi: 10.3390/atmos11040341

Determan, J. R., Budzien, S. A., Kowalski, M. P., Lovellette, M. N., Ray, P. S., Wolff, M. T., … Bandyopadhyay, R. (2007, June). Measuring atmospheric density with X-ray occultation sounding. *Journal of Geophysical Research (Space Physics)*, *112*(A6), A06323. doi: 10.1029/2006JA012014

Emmert, J. T. (2015, September). Thermospheric mass density: A review. *Advances in Space Research*, *56*(5), 773-824. doi: 10.1016/j.asr.2015.05.038

Gendreau, K. C., Arzoumanian, Z., Adkins, P. W., Albert, C. L., Anders, J. F., Aylward, A. T., … Yu, W. H. (2016, July). The Neutron star Interior Composition Explorer (NICER): design and development. In *Space telescopes and instrumentation 2016: Ultraviolet to gamma ray* (Vol. 9905, p. 99051H). doi: 10.1117/12.2231304

Hagino, K., Nakazawa, K., Sato, G., Kokubun, M., Enoto, T., Fukazawa, Y., … HXI Team (2018, April). In-orbit performance and calibration of the Hard X-ray Imager onboard Hitomi (ASTRO-H). *Journal of Astronomical Telescopes, Instruments, and Systems*, *4*, 021409. doi: 10.1117/1.JATIS.4.2.021409

Harrison, F. A., Craig, W. W., Christensen, F. E., Hailey, C. J., Zhang, W. W., Boggs, S. E., … Urry, C. M. (2013, June). The Nuclear Spectroscopic Telescope Array (NuSTAR) High-energy X-Ray Mission. *The Astrophysical Journal*, *770*(2), 103. doi: 10.1088/0004-637X/770/2/103

Hays, P. B., Roble, R. G., & Shah, A. N. (1972, May). Terrestrial Atmospheric Composition from Stellar Occultations. *Science*, *176*(4036), 793-794. doi: 10.1126/science.176.4036.793

Ishisaki, Y., Ezoe, Y., Yamada, S., Ichinohe, Y., Fujimoto, R., Takei, Y., … Szymkowiak, A. E. (2018, December). Resolve Instrument on X-ray Astronomy Recovery Mission (XARM). *Journal of Low Temperature Physics*, *193*(5-6), 991-995. doi: 10.1007/s10909-018-1913-4

Keating, G. M., Tolson, R. H., & Bradford, M. S. (2000, May). Evidence of long term global decline in the Earth's thermospheric densities apparently related to anthropogenic effects. *Geophysical Research Letters*, *27*(10), 1523-1526. doi: 10.1029/2000GL003771

Koyama, K., Tsunemi, H., Dotani, T., Bautz, M. W., Hayashida, K., Tsuru, T. G., … Awaki, H. (2007, January). X-Ray Imaging Spectrometer (XIS) on Board Suzaku. *Publications of the Astronomical Society of Japan*, *59*, 23-33. doi: 10.1093/pasj/59.sp1.S23

Lumpe, J. D., Floyd, L. E., Herring, L. C., Gibson, S. T., & Lewis, B. R. (2007, August). Measurements of thermospheric molecular oxygen from the Solar Ultraviolet Spectral Irradiance Monitor. *Journal of Geophysical Research (Atmospheres)*, *112*(D16), D16308. doi: 10.1029/2006JD008076

Makino, F., & ASTRO-C Team. (1987, January). The X-ray Astronomy Satellite ASTRO-C. *Astrophysical Letters*, *25*, 223.

Matsumoto, H., Awaki, H., Ishida, M., Furuzawa, A., Yamauchi, S., Maeda, Y., … Tawara, Y. (2018, January). Inorbit performance of the Hard X-ray Telescope (HXT) on board the Hitomi (ASTRO-H) satellite. *Journal of Astronomical Telescopes, Instruments, and Systems*, *4*, 011212. doi:

10.1117/1.JATIS.4.1.011212
Meier, R. R., Feldman, U., Brown, C. M., & Picone, J. M. (1992, August). Absolute O and O $_2$ concentrations in the thermosphere from SKYLAB occultation data. *Planetary and Space Science*, *40*(8), 1153-1166. doi: 10.1016/0032-0633(92)90042-M
Meier, R. R., Picone, J. M., Drob, D., Bishop, J., Emmert, J. T., Lean, J. L., ... Gibson, S. T. (2015, January). Remote Sensing of Earth's Limb by TIMED/GUVI: Retrieval of thermospheric composition and temperature. *Earth and Space Science*, *2*(1), 1-37. doi: 10.1002/2014EA000035
Mitsuda, K., Bautz, M., Inoue, H., Kelley, R. L., Koyama, K., Kunieda, H., ... Yoshida, A. (2007, January). The X-Ray Observatory Suzaku. *Publications of the Astronomical Society of Japan*, *59*, S1-S7. doi: 10.1093/pasj/59.sp1.S1
Mori, K., Tsunemi, H., Katayama, H., Burrows, D. N., Garmire, G. P., & Metzger, A. E. (2004, June). An X-Ray Measurement of Titan's Atmospheric Extent from Its Transit of the Crab Nebula. *The Astrophysical Journal*, *607*(2), 1065-1069. doi: 10.1086/383521
Nakazawa, K., Sato, G., Kokubun, M., Enoto, T., Fukazawa, Y., Hagino, K., ... Yuasa, T. (2018, April). Hard x-ray imager onboard Hitomi (ASTRO-H). *Journal of Astronomical Telescopes, Instruments, and Systems*, *4*, 021410. doi: 10.1117/1.JATIS.4.2.021410
Norton, R. B., & Warnock, J. M. (1968, September). Seasonal variation of molecular oxygen near 100 kilometers. *Journal of Geophysical Research*, *73*(17), 5798-5800. doi: 10.1029/JA073i017p05798
Oberheide, J., Forbes, J. M., Zhang, X., & Bruinsma, S. L. (2011, November). Climatology of upward propagating diurnal and semidiurnal tides in the thermosphere. *Journal of Geophysical Research (Space Physics)*, *116*(A11), A11306. doi: 10.1029/2011JA016784
Picone, J. M., Hedin, A. E., Drob, D. P., & Aikin, A. C. (2002, December). NRLMSISE-00 empirical model of the atmosphere: Statistical comparisons and scientific issues. *Journal of Geophysical Research (Space Physics)*, *107*(A12), 1468. doi: 10.1029/2002JA009430
Roble, R. G., & Dickinson, R. E. (1989, December). How will changes in carbon dioxide and methane modify the mean structure of the mesosphere and thermosphere? *Geophysical Research Letters*, *16*(12), 1441-1444. doi: 10.1029/GL016i012p01441
Roble, R. G., & Hays, P. B. (1972, October). A technique for recovering the vertical number density profile of atmospheric gases from planetary occultation data. *Planetary and Space Science*, *20*(10), 1727-1744. doi: 10.1016/0032-0633(72)90194-8
Serlemitsos, P. J., Soong, Y., Chan, K.-W., Okajima, T., Lehan, J. P., Maeda, Y., ... Misaki, K. (2007, January). The X-Ray Telescope onboard Suzaku. *Publications of the Astronomical Society of Japan*, *59*, S9-S21. doi: 10.1093/pasj/59.sp1.S9
Stober, G., Matthias, V., Brown, P., & Chau, J. L. (2014, October). Neutral density variation from specular meteor echo observations spanning one solar cycle. *Geophysical Research Letters*, *41*(19), 6919-6925. doi: 10.1002/2014GL061273
Takahashi, T., Kokubun, M., Mitsuda, K., Kelley, R. L., Ohashi, T., Aharonian, F., ... Zoghbi, A. (2018, April). Hitomi (ASTRO-H) X-ray Astronomy Satellite. *Journal of Astronomical Telescopes, Instruments, and Systems*, *4*, 021402. doi: 10.1117/1.JATIS.4.2.021402
Tanaka, Y., Inoue, H., & Holt, S. S. (1994, June). The X-Ray Astronomy Satellite ASCA. *Publications of the Astronomical Society of Japan*, *46*, L37-L41.
Tashiro, M., Maejima, H., Toda, K., Kelley, R., Reichenthal, L., Lobell, J., ... Irina, Z. (2018, July). Concept of the X-ray Astronomy Recovery Mission. In *Space telescopes and instrumentation 2018: Ultraviolet to gamma ray* (Vol. 10699,

p. 1069922). doi: 10.1117/12.2309455

Thiemann, E. M. B., Dominique, M., Pilinski, M. D., & Eparvier, F. G. (2017, December). Vertical Thermospheric Density Profiles From EUV Solar Occultations Made by PROBA2 LYRA for Solar Cycle 24. *Space Weather*, *15*(12), 1649-1660. doi: 10.1002/2017SW001719

Verner, D. A., Ferland, G. J., Korista, K. T., & Yakovlev, D. G. (1996, July). Atomic Data for Astrophysics. II. New Analytic FITS for Photoionization Cross Sections of Atoms and Ions. *The Astrophysical Journal*, *465*, 487. doi: 10.1086/177435

Wilms, J., Allen, A., & McCray, R. (2000, October). On the Absorption of X-Rays in the Interstellar Medium. *The Astrophysical Journal*, *542*(2), 914-924. doi: 10.1086/317016

Wood, K. S., & Ray, P. S. (2017, December). The NRL Program in X-ray Navigation. *arXiv e-prints*, arXiv:1712.03832.

Yamada, S., Uchiyama, H., Dotani, T., Tsujimoto, M., Katsuda, S., Makishima, K., … Bamba, A. (2012, June). Data-Oriented Diagnostics of Pileup Effects on the Suzaku XIS. *Publications of the Astronomical Society of Japan*, *64*, 53. doi: 10.1093/pasj/64.3.53

Table 1: Summary of occultations of the Crab nebula analyzed in this paper.

Instrument (Obs.ID)	ELV=5° (0°) → ELV=0° (5°) (UT)	Tangent point Lat, Long (°)	Occultation #, type	ΔELV1 (°)	ΔELV2 (°)
Suzaku/XIS (100023010)	2005-09-15, 14:10:54 → 12:15	20.15, 138.34	1, Rising	0.112	0.099
	2005-09-15, 15:46:51 → 48:11	20.32, 114.19	2, Rising	0.021	
	2005-09-15, 17:22:47 → 24:07	20.50, 90.04	3, Rising	0.022	
	2005-09-15, 18:21:48 → 23:08	-20.33, 255.13	4, Setting	0.022	
	2005-09-15, 18:58:43 → 19:00:03	20.67, 65.89	5, Rising	0.023	
Suzaku/XIS (100023020)	2005-09-15, 19:57:44 → 59:05	-20.42, 231.08	6, Setting	0.112	0.044
	2005-09-15, 20:34:40 → 36:00	20.86, 41.76	7, Rising	0.024	
	2005-09-15, 21:33:41 → 35:01	-20.51, 207.00	8, Setting	0.113	
	2005-09-15, 22:10:36 → 11:56	21.03, 377.60	9, Rising	0.024	
	2005-09-15, 23:09:37 → 10:57	-20.59, 182.93	10, Setting	0.113	
	2005-09-15, 23:46:32 → 47:53	21.21, 353.45	11, Rising	0.025	
	2005-09-16, 00:45:33 → 46:53	-20.67, 158.85	12, Setting	0.114	
	2005-09-16, 01:22:28 → 23:49	21.38, 329.30	13, Rising	0.026	
Suzaku/XIS (101011060)	2006-09-18, 21:33:13 → 35:13	-4.10, 35.39	14, Rising	0.022	0.180
	2006-09-18, 22:37:00 → 38:59	39.49, 219.20	15, Setting	0.134	
Suzaku/XIS (102019010)	2007-03-20, 11:03:10 → 04:30	26.95, 201.86	16, Setting	0.051	0.045
	2007-03-20, 18:03:35 → 04:56	-22.60, 273.36	17, Rising	0.128	
	2007-03-20, 19:02:39 → 03:59	26.21, 81.16	18, Setting	0.047	
	2007-03-20, 19:39:29 → 40:50	-22.55, 249.31	19, Rising	0.128	
	2007-03-20, 20:38:32 → 39:53	26.06, 57.02	20, Setting	0.047	
	2007-03-20, 21:15:23 → 16:44	-22.50, 225.25	21, Rising	0.128	
	2007-03-20, 22:14:26 → 15:46	25.90, 32.88	22, Setting	0.046	
	2007-03-20, 22:51:17 → 52:37	-22.46, 201.20	23, Rising	0.127	
	2007-03-20, 23:50:20 → 51:40	25.75, 8.73	24, Setting	0.045	
	2007-03-21, 00:27:11 → 28:31	-22.41, 177.14	25, Rising	0.127	
	2007-03-21, 01:26:14 → 27:34	25.60, -15.41	26, Setting	0.044	
	2007-03-21, 02:03:05 → 04:25	-22.36, 153.08	27, Rising	0.126	
	2007-03-21, 03:02:07 → 03:28	25.44, 320.45	28, Setting	0.044	
	2007-03-21, 03:38:59 → 40:19	-22.31, 129.03	29, Rising	0.126	
	2007-03-21, 04:38:01 → 39:22	25.29, 296.31	30, Setting	0.043	
	2007-03-21, 05:14:53 → 16:13	-22.26, 104.97	31, Rising	0.126	
	2007-03-21, 06:13:55 → 15:15	25.13, 272.17	32, Setting	0.042	
	2007-03-21, 06:50:47 → 52:07	-22.20, 80.91	33, Rising	0.125	
	2007-03-21, 07:49:49 → 51:09	24.98, 248.02	34, Setting	0.041	
	2007-03-21, 08:26:41 → 28:01	-22.15, 56.86	35, Rising	0.125	
	2007-03-21, 09:25:43 → 27:03	24.82, 223.88	36, Setting	0.041	
	2007-03-21, 10:02:35 → 03:55	-22.09, 32.80	37, Rising	0.124	
Suzaku/XIS (103007010)	2008-08-27, 08:53:07 → 54:28	8.72, 242.16	38, Rising	0.000	0.103
	2008-08-27, 10:29:01 → 30:21	8.93, 218.03	39, Rising	0.000	
	2008-08-27, 12:04:54 → 06:15	9.13, 193.90	40, Rising	0.000	
	2008-08-27, 13:03:58 → 05:19	-13.06, -4.74	41, Setting	0.065	
	2008-08-27, 13:40:47 → 42:08	9.34, 169.78	42, Rising	0.000	
	2008-08-27, 15:16:41 → 18:01	9.54, 145.65	43, Rising	0.000	
	2008-08-27, 16:52:34 → 53:55	9.74, 121.53	44, Rising	0.000	
	2008-08-27, 18:28:27 → 29:48	9.94, 97.40	45, Rising	0.000	
	2008-08-27, 19:27:31 → 28:51	-13.67, 258.93	46, Setting	0.069	
	2008-08-27, 20:04:20 → 05:41	10.15, 73.27	47, Rising	0.001	
	2008-08-27, 21:03:24 → 04:44	-13.82, 234.84	48, Setting	0.070	
	2008-08-27, 21:40:14 → 41:34	10.35, 49.14	49, Rising	0.001	

To be continued

Instrument (Obs.ID)	ELV=5° (0°) → ELV=0° (5°) (UT)	Tangent point Lat, Long (°)	Occultation #, type	ΔELV (°)	(°)
	2008-08-27, 22:39:17 → 40:37	-13.96, 210.76	50, Setting	0.070	
	2008-08-28, 00:15:10 → 16:30	-14.11, 186.67	51, Setting	0.071	
	2008-08-28, 00:52:00 → 53:21	10.76, 360.88	52, Rising	0.001	
	2008-08-28, 01:51:03 → 52:23	-14.26, 162.59	53, Setting	0.072	
	2008-08-28, 02:27:53 → 29:14	10.96, 336.76	54, Rising	0.001	
	2008-08-28, 03:26:56 → 28:17	-14.40, 138.51	55, Setting	0.073	
	2008-08-28, 04:03:46 → 05:07	11.16, 312.63	56, Rising	0.001	
	2008-08-28, 05:02:49 → 04:10	-14.55, 114.43	57, Setting	0.074	
	2010-04-05, 14:04:46 → 06:41	-7.07, 124.44	58, Setting	0.034	
	2010-04-05, 15:40:40 → 42:36	-6.81, 100.49	59, Setting	0.033	
	2010-04-05, 17:16:35 → 18:31	-6.54, 76.53	60, Setting	0.032	
	2010-04-05, 18:52:29 → 54:26	-6.28, 52.58	61, Setting	0.031	
	2010-04-05, 19:25:03 → 27:00	39.64, 205.07	62, Rising	0.135	
	2010-04-05, 20:28:24 → 30:21	-6.01, 28.63	63, Setting	0.030	
	2010-04-05, 21:00:55 → 02:52	39.62, 181.05	64, Rising	0.135	
	2010-04-05, 22:04:18 → 06:16	-5.73, 4.68	65, Setting	0.029	
	2010-04-05, 22:36:46 → 38:44	39.61, 157.04	66, Rising	0.134	
	2010-04-06, 00:12:38 → 14:36	39.59, 133.03	67, Rising	0.134	
Suzaku/XIS (105002010)	2010-04-06, 01:48:29 → 50:28	39.57, 109.02	68, Rising	0.134	0.030
	2010-04-06, 03:24:21 → 26:20	39.55, 85.01	69, Rising	0.134	
	2010-04-06, 05:00:12 → 02:12	39.52, 61.00	70, Rising	0.134	
	2010-04-06, 06:03:51 → 05:51	-4.34, 244.94	71, Setting	0.023	
	2010-04-06, 06:36:04 → 38:04	39.49, 36.99	72, Rising	0.134	
	2010-04-06, 07:39:46 → 41:47	-4.06, 220.99	73, Setting	0.022	
	2010-04-06, 08:11:55 → 13:56	39.46, 373.00	74, Rising	0.133	
	2010-04-06, 09:15:41 → 17:42	-3.77, 197.05	75, Setting	0.021	
	2010-04-06, 09:47:47 → 49:48	39.43, 349.00	76, Rising	0.133	
	2010-04-06, 10:51:36 → 53:37	-3.47, 173.12	77, Setting	0.020	
	2010-04-06, 11:23:39 → 25:40	39.40, 325.00	78, Rising	0.133	
	2011-09-01, 06:38:29 → 40:44	37.85, 252.57	79, Rising	0.122	
	2011-09-01, 07:43:43 → 45:58	5.22, 77.84	80, Setting	0.001	
	2011-09-01, 08:14:19 → 16:34	37.75, 228.67	81, Rising	0.121	
	2011-09-01, 09:19:36 → 21:52	5.56, 53.94	82, Setting	0.001	
	2011-09-01, 09:50:09 → 52:24	37.66, 204.74	83, Rising	0.120	
	2011-09-01, 10:55:28 → 57:45	5.91, 30.05	84, Setting	0.001	
	2011-09-01, 11:25:58 → 28:14	37.56, 180.81	85, Rising	0.120	
	2011-09-01, 12:31:21 → 33:38	6.26, 6.16	86, Setting	0.001	
	2011-09-01, 13:01:47 → 04:04	37.47, 156.89	87, Rising	0.119	
	2011-09-01, 14:37:37 → 39:54	37.37, 132.96	88, Rising	0.118	
	2011-09-01, 16:13:26 → 15:44	37.27, 109.04	89, Rising	0.117	
	2011-09-01, 17:49:16 → 51:34	37.16, 85.12	90, Rising	0.117	
	2011-09-01, 18:54:51 → 57:10	7.65, 270.61	91, Setting	0.000	
Suzaku/XIS (106012010)	2011-09-01, 19:25:05 → 27:24	37.05, 61.20	92, Rising	0.116	0.105
	2011-09-01, 20:30:44 → 33:04	8.01, 246.73	93, Setting	0.000	
	2011-09-01, 21:00:55 → 03:14	36.94, 37.29	94, Rising	0.115	
	2011-09-01, 22:06:37 → 08:57	8.36, 222.84	95, Setting	0.000	
	2011-09-01, 22:36:45 → 39:05	36.82, 373.39	96, Rising	0.114	
	2011-09-01, 23:42:30 → 44:50	8.72, 198.96	97, Setting	0.000	
	2011-09-02, 00:12:35 → 14:55	36.71, 349.47	98, Rising	0.113	
	2011-09-02, 01:18:23 → 20:44	9.08, 175.09	99, Setting	0.000	
	2011-09-02, 01:48:25 → 50:45	36.59, 325.57	100, Rising	0.112	
	2011-09-02, 02:54:16 → 56:37	9.43, 151.20	101, Setting	0.000	

To be continued

Instrument (Obs.ID)	ELV=5° (0°) → ELV=0° (5°) (UT)	Tangent point Lat, Long (°)	Occultation #, type	ΔELV (°)	(°)
	2011-09-02, 03:24:14 → 26:36	36.47, 301.66	102, Rising	0.112	
	2011-09-02, 04:30:09 → 32:30	9.78, 127.32	103, Setting	0.000	
	2011-09-02, 05:00:04 → 02:26	36.34, 277.76	104, Rising	0.111	
	2011-09-02, 06:06:02 → 08:24	10.14, 103.45	105, Setting	0.000	
Suzaku/XIS (106014010)	2012-03-14, 01:27:03 → 28:23	20.44, -12.64	106, Setting	0.022	0.226
	2012-03-14, 02:03:59 → 05:18	-20.09, 158.74	107, Rising	0.112	
	2012-03-14, 03:02:46 → 04:06	20.26, 323.26	108, Setting	0.022	
	2012-03-14, 03:39:42 → 41:01	-20.00, 134.72	109, Rising	0.111	
	2012-03-14, 04:38:29 → 39:49	20.09, 299.17	110, Setting	0.021	
	2012-03-14, 05:15:25 → 16:44	-19.91, 110.70	111, Rising	0.111	
	2012-03-14, 05:15:25 → 16:44	-19.91, 110.70	112, Rising	0.020	
	2012-03-14, 06:14:12 → 15:32	19.91, 275.08	113, Setting	0.020	
	2012-03-14, 06:51:08 → 52:27	-19.82, 86.67	114, Rising	0.110	
	2012-03-14, 07:49:55 → 51:15	19.73, 250.98	115, Setting	0.020	
	2012-03-14, 08:26:51 → 28:10	-19.72, 62.65	116, Rising	0.109	
	2012-03-14, 09:25:38 → 26:58	19.55, 226.88	117, Setting	0.019	
	2012-03-14, 11:01:21 → 02:41	19.37, 202.79	118, Setting	0.019	
	2012-03-14, 12:37:04 → 38:24	19.19, 178.70	119, Setting	0.018	
	2012-03-14, 14:12:47 → 14:07	19.01, 154.60	120, Setting	0.017	
	2012-03-14, 15:48:30 → 49:50	18.82, 130.51	121, Setting	0.016	
	2012-03-14, 17:24:13 → 25:33	18.64, 106.41	122, Setting	0.016	
	2012-03-14, 18:01:09 → 02:29	-19.13, 278.51	123, Rising	0.105	
	2012-03-14, 18:59:56 → 19:01:16	18.46, 82.32	124, Setting	0.016	
	2012-03-14, 19:36:52 → 38:12	-19.02, 254.49	125, Rising	0.104	
	2012-03-14, 20:35:39 → 36:59	18.28, 58.23	126, Setting	0.015	
	2012-03-14, 21:12:35 → 13:55	-18.92, 230.46	127, Rising	0.104	
	2012-03-14, 22:11:22 → 12:42	18.09, 34.13	128, Setting	0.015	
	2012-03-14, 22:48:18 → 49:38	-18.81, 206.43	129, Rising	0.103	
	2012-03-14, 23:47:05 → 48:25	17.90, 10.03	130, Setting	0.014	
	2012-03-15, 00:24:01 → 25:21	-18.71, 182.40	131, Rising	0.102	
	2012-03-15, 01:22:49 → 24:09	17.72, -14.06	132, Setting	0.014	
	2012-03-15, 01:59:44 → 02:01:04	-18.60, 158.37	133, Rising	0.101	
	2012-03-15, 02:58:32 → 59:52	17.53, 321.84	134, Setting	0.013	
Suzaku/XIS (107011010)	2012-09-26, 06:03:29 → 05:09	-15.90, 70.09	135, Setting	0.083	0.099
	2012-09-26, 06:38:02 → 39:41	39.05, 226.54	136, Rising	0.132	
	2012-09-26, 07:39:11 → 40:50	-15.73, 46.15	137, Setting	0.082	
	2012-09-26, 08:13:41 → 15:20	39.09, 202.52	138, Rising	0.133	
	2012-09-26, 09:49:20 → 51:00	39.12, 178.50	139, Rising	0.133	
	2012-09-26, 11:24:59 → 26:39	39.16, 154.48	140, Rising	0.133	
	2012-09-26, 13:00:39 → 02:19	39.19, 130.46	141, Rising	0.133	
	2012-09-26, 14:36:18 → 37:58	39.23, 106.44	142, Rising	0.134	
	2012-09-26, 16:11:57 → 13:38	39.26, 82.43	143, Rising	0.134	
	2012-09-26, 17:13:19 → 15:01	-14.69, 262.54	144, Setting	0.075	
	2012-09-26, 17:47:36 → 49:17	39.29, 58.41	145, Rising	0.134	
	2012-09-26, 18:49:00 → 50:42	-14.51, 238.61	146, Setting	0.074	
	2012-09-26, 19:23:15 → 24:57	39.32, 34.39	147, Rising	0.134	
	2012-09-26, 20:24:42 → 26:24	-14.32, 214.67	148, Setting	0.073	
	2012-09-26, 20:58:54 → 21:00:36	39.35, 370.38	149, Rising	0.135	
	2012-09-26, 22:00:24 → 02:06	-14.13, 190.75	150, Setting	0.072	
	2012-09-26, 22:34:34 → 36:16	39.38, 346.37	151, Rising	0.135	
	2012-09-26, 23:36:05 → 37:48	-13.94, 166.82	152, Setting	0.070	
	2012-09-27, 00:10:13 → 11:56	39.41, 322.36	153, Rising	0.135	

To be continued

Instrument (Obs.ID)	ELV=5° (0°) → ELV=0° (5°) (UT)	Tangent point Lat, Long (°)	Occultation #, type	ΔELV (°)	(°)
	2012-09-27, 01:11:47 → 13:30	-13.75, 142.89	154, Setting	0.069	
	2012-09-27, 01:45:52 → 47:35	39.43, 298.35	155, Rising	0.135	
	2012-09-27, 02:47:29 → 49:12	-13.56, 118.96	156, Setting	0.068	
	2012-09-27, 03:21:32 → 23:15	39.46, 274.34	157, Rising	0.135	
	2012-09-27, 04:23:10 → 24:54	-13.37, 95.03	158, Setting	0.067	
	2012-09-27, 04:57:11 → 58:54	39.48, 250.33	159, Rising	0.136	
Suzaku/XIS (107012010)	2013-02-27, 00:31:45 → 33:05	-10.92, 2.88	160, Setting	0.054	0.150
	2013-02-27, 01:08:35 → 09:56	6.87, 178.27	161, Rising	0.000	
	2013-02-27, 02:44:12 → 45:33	7.08, 154.22	162, Rising	0.000	
	2013-02-27, 04:19:49 → 21:10	7.28, 130.16	163, Rising	0.000	
	2013-02-27, 05:55:26 → 56:47	7.49, 106.11	164, Rising	0.000	
	2013-02-27, 07:31:03 → 32:24	7.70, 82.05	165, Rising	0.000	
	2013-02-27, 08:29:49 → 31:10	-11.75, 242.77	166, Setting	0.058	
	2013-02-27, 09:06:40 → 08:01	7.90, 57.99	167, Rising	0.000	
	2013-02-27, 10:05:26 → 06:46	-11.91, 218.75	168, Setting	0.059	
	2013-02-27, 10:42:17 → 43:38	8.11, 33.93	169, Rising	0.000	
	2013-02-27, 11:41:03 → 42:23	-12.07, 194.73	170, Setting	0.060	
	2013-02-27, 13:16:39 → 18:00	-12.23, 170.71	171, Setting	0.061	
	2013-02-27, 13:53:31 → 54:52	8.52, 345.82	172, Rising	0.000	
	2013-02-27, 14:52:16 → 53:37	-12.39, 146.69	173, Setting	0.062	
	2013-02-27, 15:29:08 → 30:28	8.72, 321.76	174, Rising	0.000	
	2013-02-27, 16:27:53 → 29:13	-12.55, 122.67	175, Setting	0.063	
	2013-02-27, 17:04:45 → 06:05	8.93, 297.70	176, Rising	0.000	
	2013-02-27, 18:03:30 → 04:50	-12.70, 98.65	177, Setting	0.064	
	2013-02-27, 19:39:07 → 40:27	-12.86, 74.63	178, Setting	0.065	
	2013-02-27, 20:15:59 → 17:19	9.34, 249.58	179, Rising	0.000	
	2013-02-27, 21:14:43 → 16:04	-13.01, 50.61	180, Setting	0.066	
	2013-02-27, 21:51:36 → 52:56	9.54, 225.52	181, Rising	0.000	
Suzaku/XIS (108011010)	2013-09-30, 10:42:29 → 43:49	-19.32, 191.65	182, Rising	0.106	0.211
	2013-09-30, 11:41:05 → 42:24	19.01, -4.64	183, Setting	0.018	
	2013-09-30, 12:18:01 → 19:21	-19.22, 167.69	184, Rising	0.106	
	2013-09-30, 13:16:37 → 17:56	18.83, 331.31	185, Setting	0.017	
	2013-09-30, 13:53:34 → 54:53	-19.12, 143.70	186, Rising	0.105	
	2013-09-30, 14:52:09 → 53:29	18.64, 307.26	187, Setting	0.017	
	2013-09-30, 15:29:06 → 30:25	-19.02, 119.72	188, Rising	0.104	
	2013-09-30, 16:27:41 → 29:01	18.46, 283.21	189, Setting	0.016	
	2013-09-30, 17:04:38 → 05:58	-18.91, 95.74	190, Rising	0.104	
	2013-09-30, 18:03:13 → 04:33	18.28, 259.17	191, Setting	0.015	
	2013-09-30, 18:40:10 → 41:30	-18.81, 71.76	192, Rising	0.103	
	2013-09-30, 19:38:45 → 40:05	18.09, 235.12	193, Setting	0.015	
	2013-09-30, 21:14:18 → 15:37	17.90, 211.07	194, Setting	0.014	
	2013-09-30, 22:49:50 → 51:10	17.72, 187.02	195, Setting	0.014	
	2013-10-01, 00:25:22 → 26:42	17.53, 162.97	196, Setting	0.013	
	2013-10-01, 02:00:54 → 02:14	17.34, 138.93	197, Setting	0.013	
	2013-10-01, 03:36:26 → 37:46	17.16, 114.87	198, Setting	0.012	
	2013-10-01, 04:13:23 → 14:43	-18.15, 287.88	199, Rising	0.098	
	2013-10-01, 05:11:59 → 13:18	16.97, 90.83	200, Setting	0.012	
	2013-10-01, 05:48:55 → 50:15	-18.03, 263.89	201, Rising	0.097	
	2013-10-01, 06:47:31 → 48:51	16.78, 66.78	202, Setting	0.011	
	2013-10-01, 07:24:27 → 25:47	-17.92, 239.91	203, Rising	0.097	
	2013-10-01, 08:23:03 → 24:23	16.59, 42.74	204, Setting	0.011	
	2013-10-01, 08:59:59 → 09:01:19	-17.80, 215.92	205, Rising	0.096	

To be continued

Instrument (Obs.ID)	ELV=5° (0°) → ELV=0° (5°) (UT)	Tangent point Lat, Long (°)	Occultation #, type	ΔELV (°)	(°)
	2013-10-01, 09:58:35 → 59:55	16.40, 18.68	206, Setting	0.010	
Suzaku/XIS (408008010)	2013-09-16, 17:04:02 → 05:53	-9.30, 106.64	207, Rising	0.045	0.236
	2013-09-16, 18:06:21 → 08:11	39.70, 288.58	208, Setting	0.138	
	2013-09-16, 18:39:37 → 41:28	-9.54, 82.76	209, Rising	0.046	
	2013-09-16, 19:41:53 → 43:43	39.70, 264.63	210, Setting	0.138	
	2013-09-16, 20:15:12 → 17:03	-9.78, 58.87	211, Rising	0.048	
	2013-09-16, 21:17:26 → 19:15	39.70, 240.67	212, Setting	0.138	
	2013-09-16, 21:50:48 → 52:38	-10.01, 34.99	213, Rising	0.049	
	2013-09-16, 22:52:58 → 54:47	39.70, 216.72	214, Setting	0.138	
	2013-09-17, 00:28:30 → 30:19	39.69, 192.75	215, Setting	0.138	
	2013-09-17, 02:04:03 → 05:51	39.68, 168.80	216, Setting	0.137	
	2013-09-17, 03:39:35 → 41:23	39.67, 144.83	217, Setting	0.137	
Hitomi/HXI (100044010)	2016-03-25, 18:47:29 → 48:53	32.99, 167.97	218, Setting	0.086	0.069
	2016-03-25, 21:33:35 → 34:59	-22.77, 282.69	219, Rising	0.130	
	2016-03-25, 21:59:03 → 22:00:27	32.88, 143.81	220, Setting	0.085	
	2016-03-26, 01:10:37 → 12:01	32.77, 119.64	221, Setting	0.084	

End of table

Table 2. Combined N and O column number densities measured with Suzaku/XIS

ELV (deg)	Altitude (km)	Column density ($\times 10^{22}$ cm^{-2})		
		106012010	106014010	Mean (SD)[a]
4.7–5.3	202.2–224.8	$0.3(<1.9)\times10^{-5}$	$12.0\pm2.6\times10^{-5}$	7.5×10^{-5} (5.2×10^{-5})
4.4–4.7	190.6–202.2	$1.4(<2.9)\times10^{-5}$	$12.5\pm3.6\times10^{-5}$	10.4×10^{-5} (7.5×10^{-5})
4.1–4.4	178.8–190.6	$10.9\pm3.0\times10^{-5}$	$2.3\pm0.5\times10^{-4}$	16.6×10^{-5} (9.5×10^{-5})
3.8–4.1	166.9–178.8	$1.6\pm0.3\times10^{-4}$	$3.4\pm0.4\times10^{-4}$	2.7×10^{-4} (1.3×10^{-4})
3.5–3.8	154.7–166.9	$3.0\pm0.4\times10^{-4}$	$5.8\pm0.5\times10^{-4}$	4.6×10^{-4} (1.9×10^{-4})
3.4–3.5	150.6–154.7	$4.6\pm0.7\times10^{-4}$	$8.0\pm1.0\times10^{-4}$	7.6×10^{-4} (3.8×10^{-4})
3.3–3.4	146.5–150.6	$5.6\pm0.7\times10^{-4}$	$10.4\pm1.3\times10^{-3}$	7.3×10^{-4} (3.2×10^{-4})
3.2–3.3	142.4–146.5	$7.3\pm0.8\times10^{-4}$	$12.0\pm1.4\times10^{-4}$	9.6×10^{-4} (4.5×10^{-4})
3.1–3.2	138.3–142.4	$8.2\pm0.9\times10^{-4}$	$13.3\pm1.7\times10^{-4}$	12.2×10^{-4} (5.0×10^{-4})
3.0–3.1	134.1–138.3	$11.5\pm0.9\times10^{-4}$	$17.7\pm1.4\times10^{-4}$	15.3×10^{-4} (0.6×10^{-4})
2.9–3.0	129.9–134.1	$1.4\pm0.1\times10^{-3}$	$2.3\pm0.2\times10^{-3}$	2.3×10^{-3} (1.0×10^{-3})
2.8–2.9	125.7–129.9	$1.9\pm0.2\times10^{-3}$	$3.1\pm0.2\times10^{-3}$	2.7×10^{-3} (1.0×10^{-3})
2.7–2.8	121.5–125.7	$2.6\pm0.2\times10^{-3}$	$5.2\pm0.4\times10^{-3}$	4.0×10^{-3} (1.6×10^{-3})
2.6–2.7	117.3–121.5	$3.9\pm0.2\times10^{-3}$	$6.1\pm0.5\times10^{-3}$	5.5×10^{-3} (2.3×10^{-3})
2.5–2.6	113–117.3	$6.1\pm0.3\times10^{-3}$	$10.0\pm0.7\times10^{-3}$	8.6×10^{-3} (3.6×10^{-3})
2.4–2.5	108.7–113	$10.7\pm0.6\times10^{-3}$	$18.3\pm1.2\times10^{-3}$	16.6×10^{-3} (7.7×10^{-3})
2.3–2.4	104.4–108.7	0.020 ± 0.01	0.037 ± 0.005	0.029 (0.013)
2.2–2.3	100.1–104.4	0.054 ± 0.004	$0.092^{+0.015}_{-0.012}$	0.068 (0.037)
2.1–2.2	95.7–100.1	$0.103^{+0.009}_{-0.008}$	$0.16^{+0.04}_{-0.03}$	0.13 (0.03)
2.0–2.1	91.4–95.7	0.23 ± 0.02	$0.30^{+0.06}_{-0.05}$	0.28 (0.14)

Table 3. Combined N and O column number densities measured with Hitomi/HXI

ELV (deg)	Altitude (km)	Column density ($\times 10^{22}$ cm^{-2})
2.0–2.1	92.7–97.1	0.20 ± 0.01
1.9–2.0	88.2–92.7	0.48 ± 0.02
1.8–1.9	83.8–88.2	1.11 ± 0.06
1.7–1.8	79.3–83.8	$2.53^{+0.17}_{-0.15}$
1.6–1.7	74.8–79.3	$5.35^{+0.47}_{-0.40}$
1.5–1.6	70.3–74.8	$14.2^{+2.7}_{-2.1}$

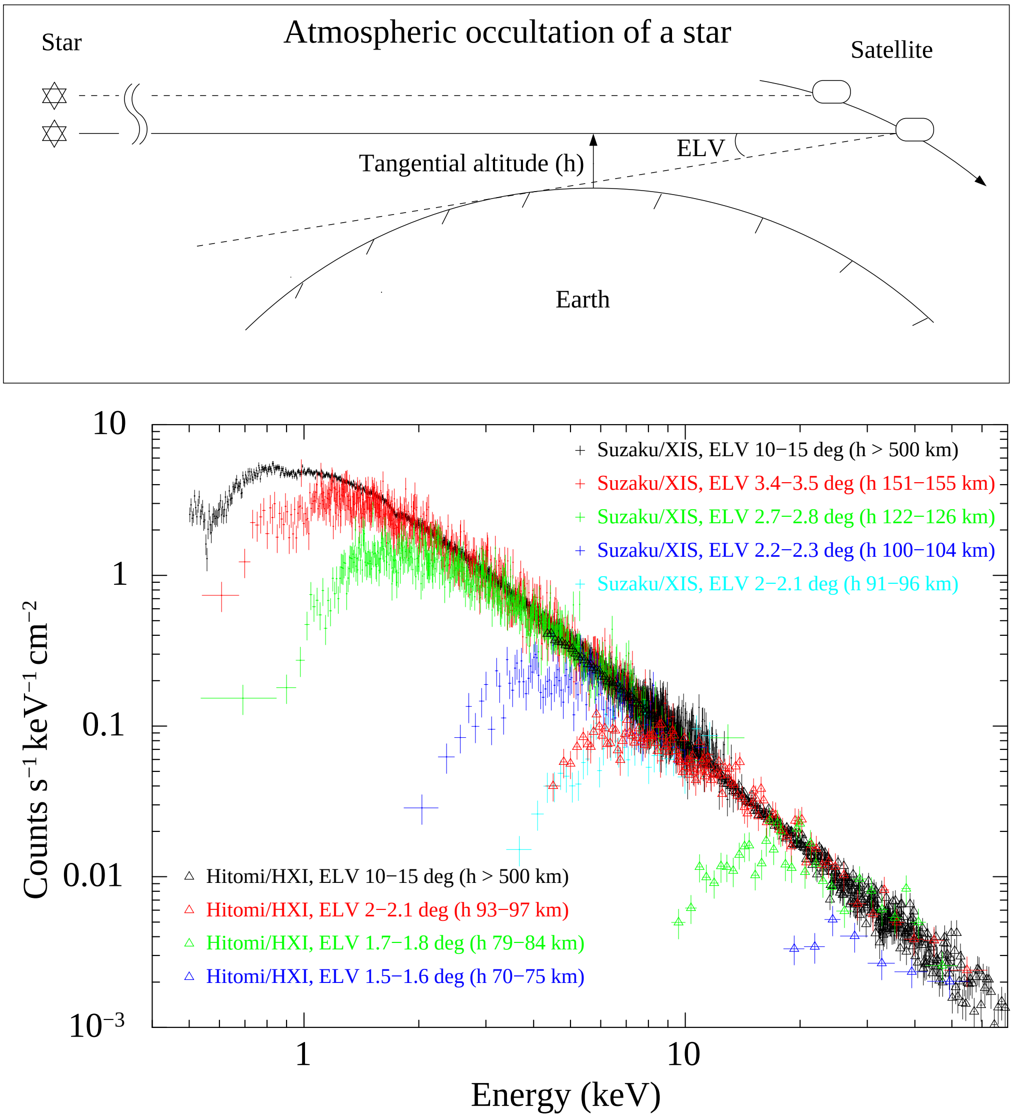

Figure 1. Upper panel: Geometry of Earth's atmospheric occultation of a star. The tangent altitude and ELV, defined as the elevation angle of the source above the Earth, are indicated. As the satellite proceeds, the source sets behind the Earth's atmosphere. Lower panel: X-ray spectral variation of the Crab nebula during the occultation. The data are taken with the XIS and HXI covering 0.4–12 keV and 4–70 keV, respectively. Spectra free from the atmospheric absorption are shown in black. As the occultation progresses, the X-ray photons are gradually absorbed from the low-energy side due to the increasing atmospheric density with the decreasing tangential altitude.

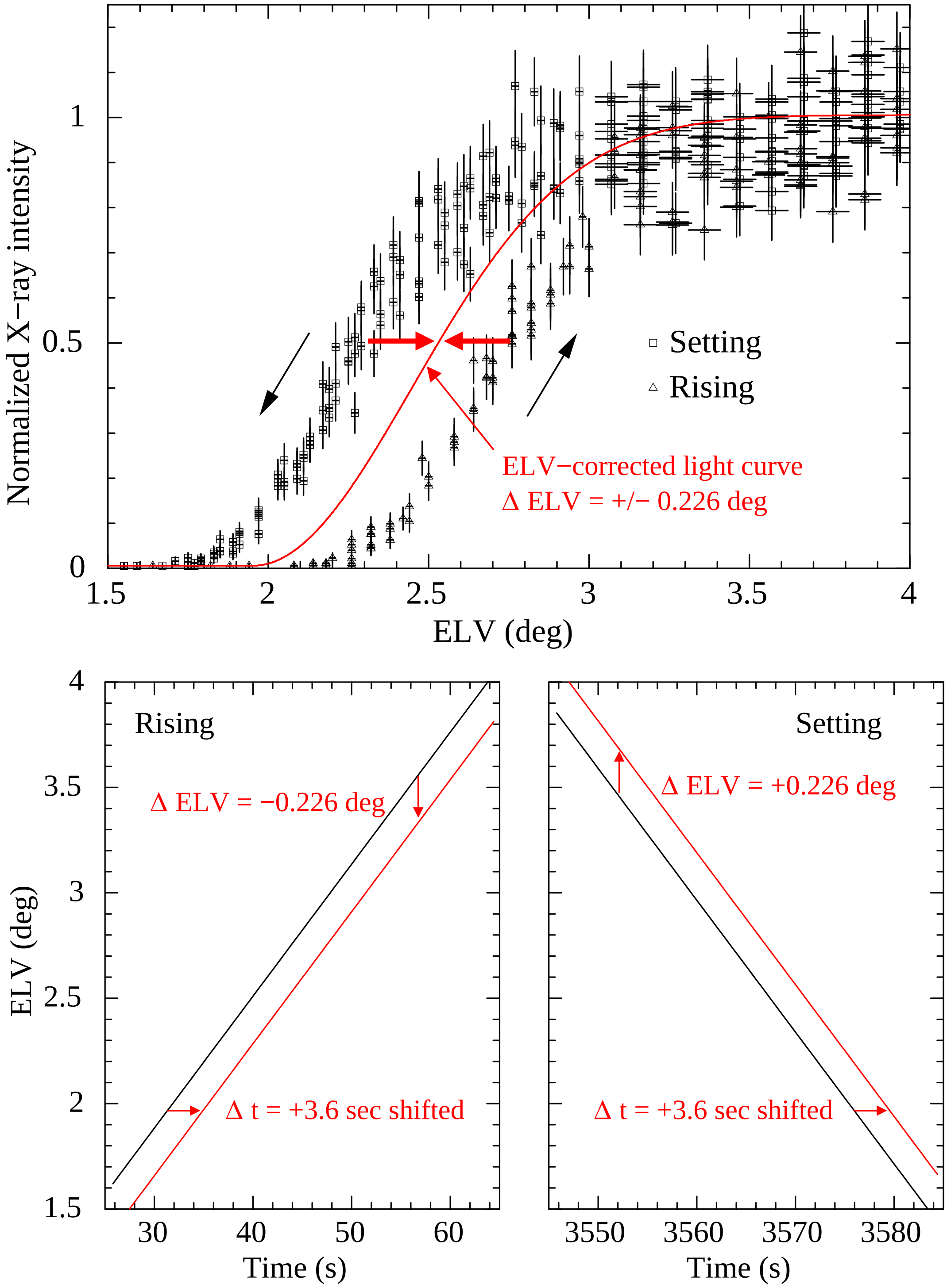

Figure 2. Upper panel: X-ray occultation light curves obtained with Suzaku/XIS, showing all the occultation data in Obs.ID 106014010. A clear ELV shift can be seen between set and rise profiles. Lower panels: Time variation of ELV during typical set (right) and rise (left) in Obs.ID 106014010. The time $t = 0$ is when the Crab nebula emerges from the solid Earth, ELV $= 0^{\circ}$. After $\sim$30 s, X-ray emission from the Crab nebula emerges from the Earth's atmosphere. After about an hour, the Crab nebula sets into the Earth. A time shift by +3.6 s will result in ELV shifts of $\pm 0.226^{\circ}$ for the set and rise, which can match the set and rise profiles in the upper panel.

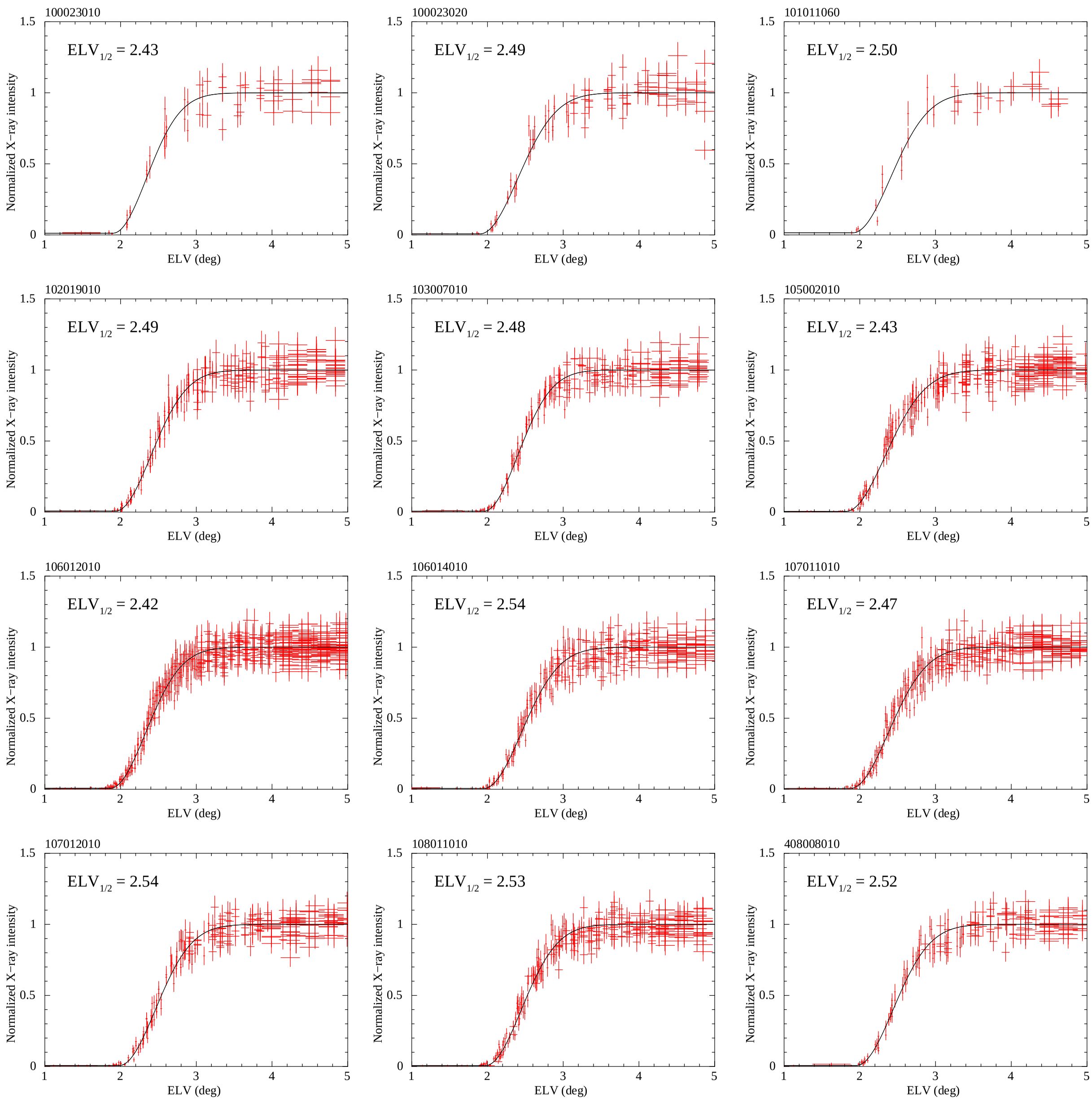

Figure 3. Occultation light curves for all the Suzaku data listed in Table 1. The intensities are normalized at the unattenuated level, and the ELV shifts between set and rise are corrected. These profiles are fitted with a phenomenological model shown in black, from which we computed $ELV_{1/2}$ values shown in the upper left corner of each panel.

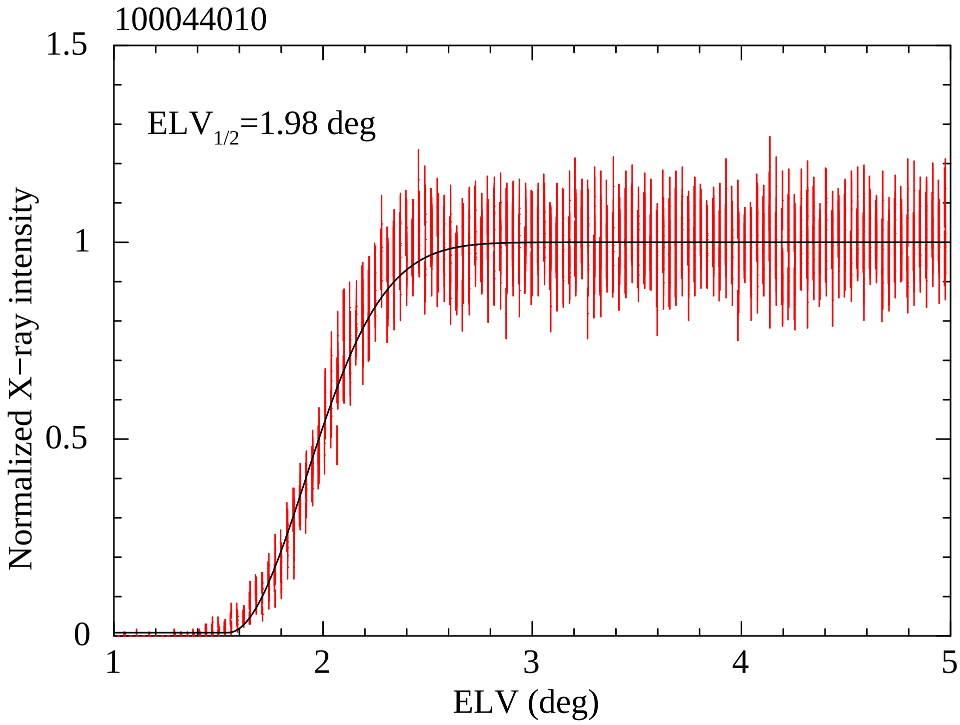

Figure 4. Same as Figure 3 but for Hitomi.

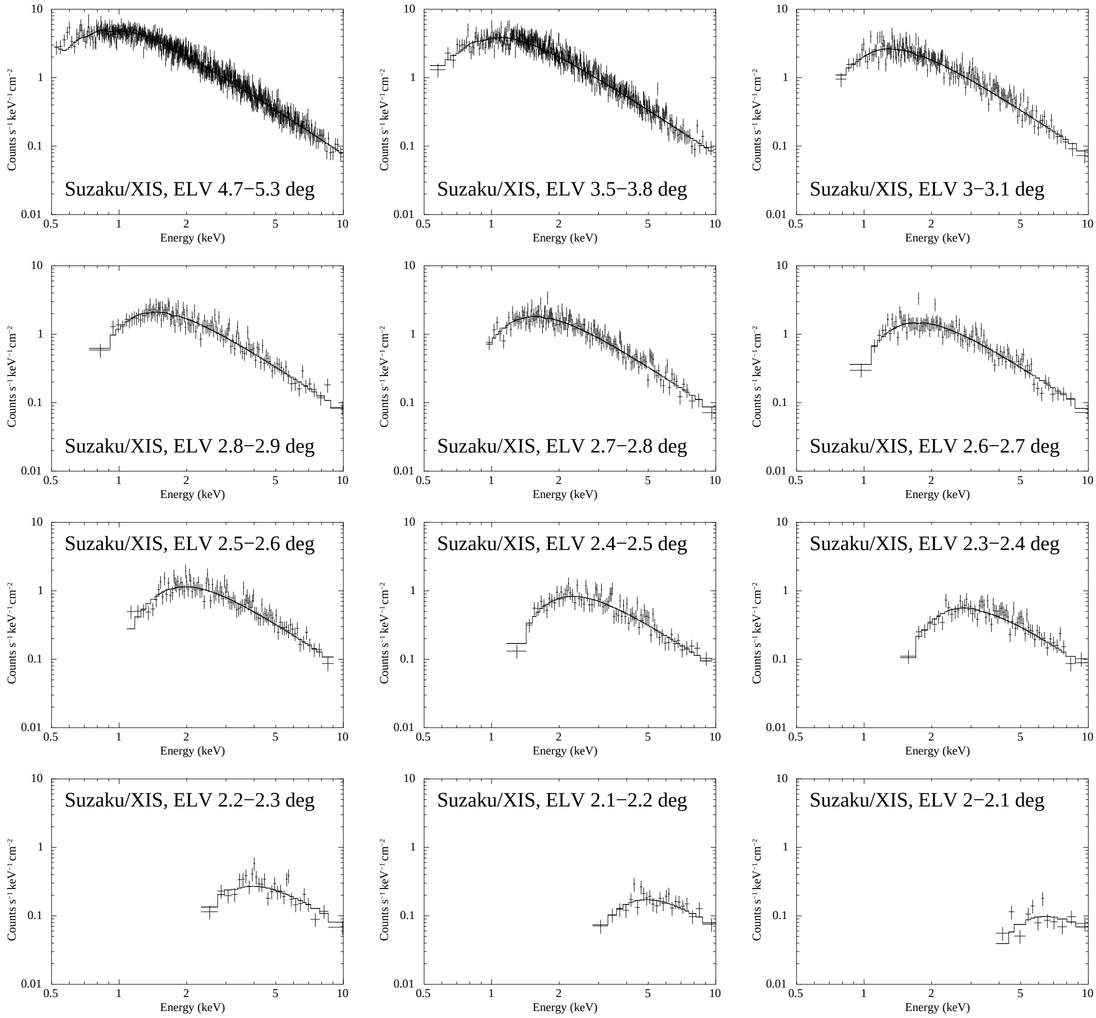

Figure 5. Example X-ray spectra obtained with the XIS (Obs.ID 106012010). The data are fitted with the emission model from the Crab nebula, which takes account of the Earth's atmospheric absorption.

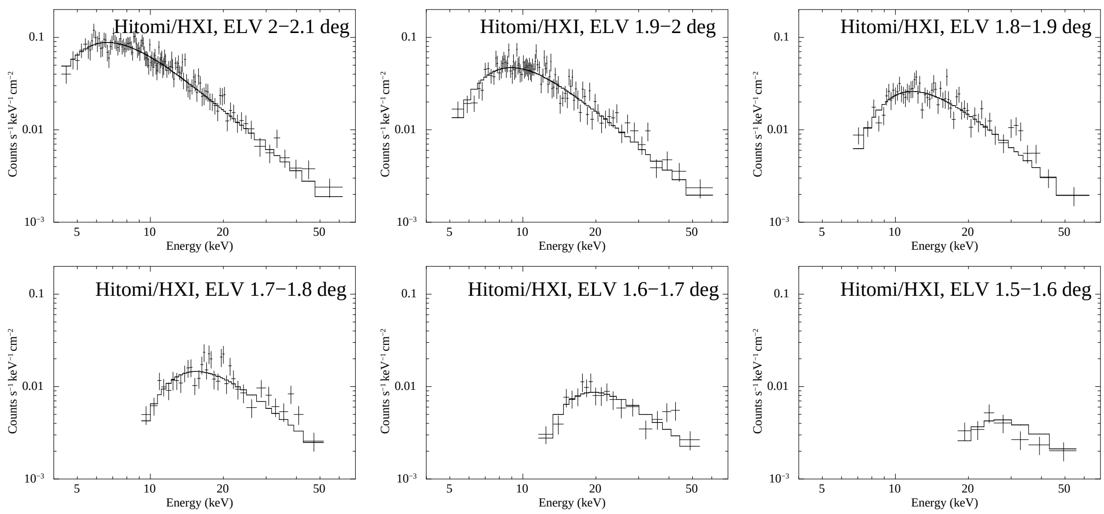

Figure 6. Same as Figure 5 but for Hitomi.

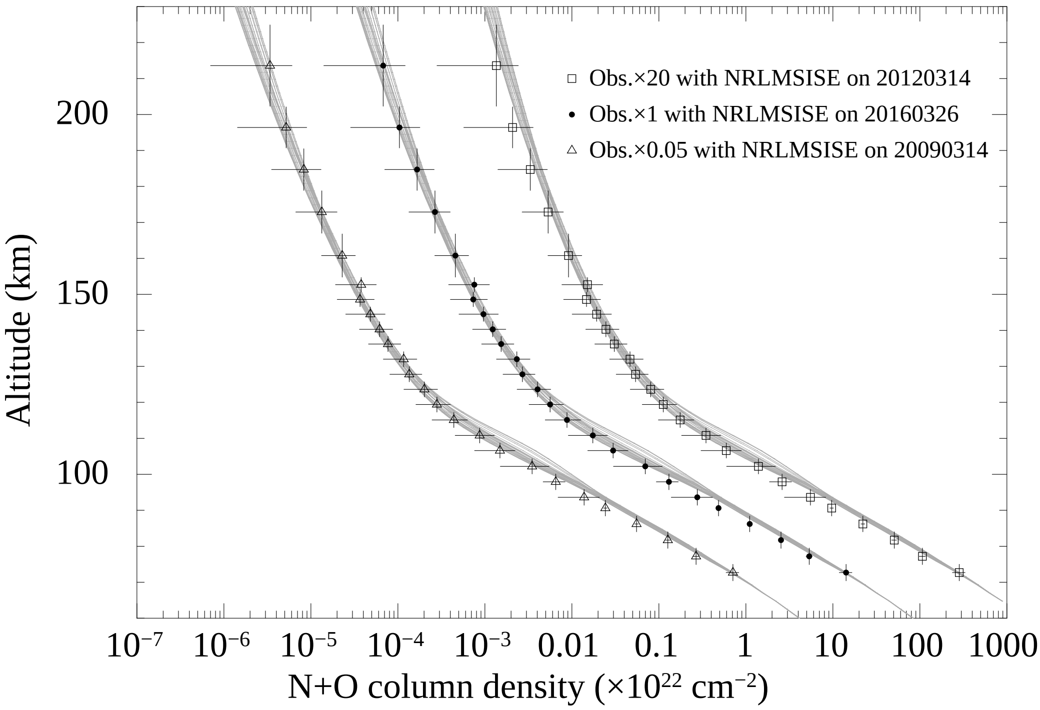

Figure 7. Atmospheric N+O column densities as a function of altitude. The bottom five data points are obtained with Hitomi/HXI, whereas other data are obtained with Suzaku/XIS, which are means and standard deviations of the ten data sets (Obs.IDs) listed in Table 2. Gray lines represent predictions of the NRLMSISE-00 model at various hours of a day. For clarity, we shift the data and model horizontally by multiplying factors of 20 (NRL model on 2012-03-14, the solar maximum) or 1/20 (NRL model on 2009-03-14, the solar minimum).

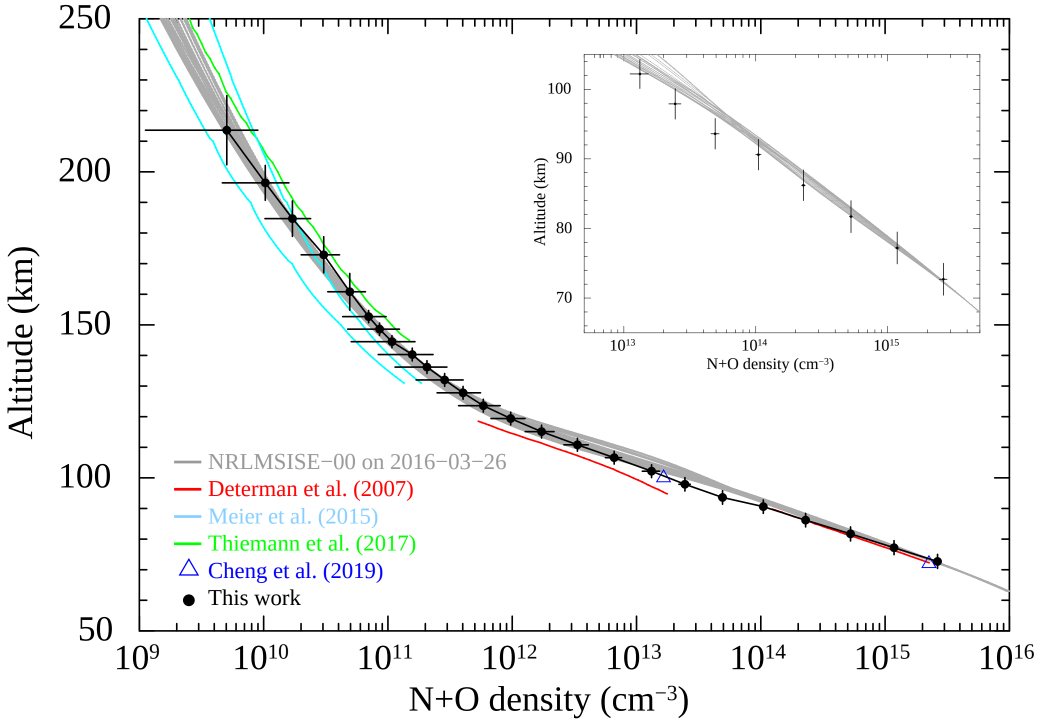

Figure 8. Atmospheric N+O densities as a function of altitude, which is inverted from the column density in Figure 7. The gray lines represent the NRLMSISE-00 models at various hours of the day 2016-03-26. Other data from recent literatures are also plotted. The inset shows a close-up view of the lowest altitudes, where our density measurements are significantly smaller than the NRLMSISE-00 model.

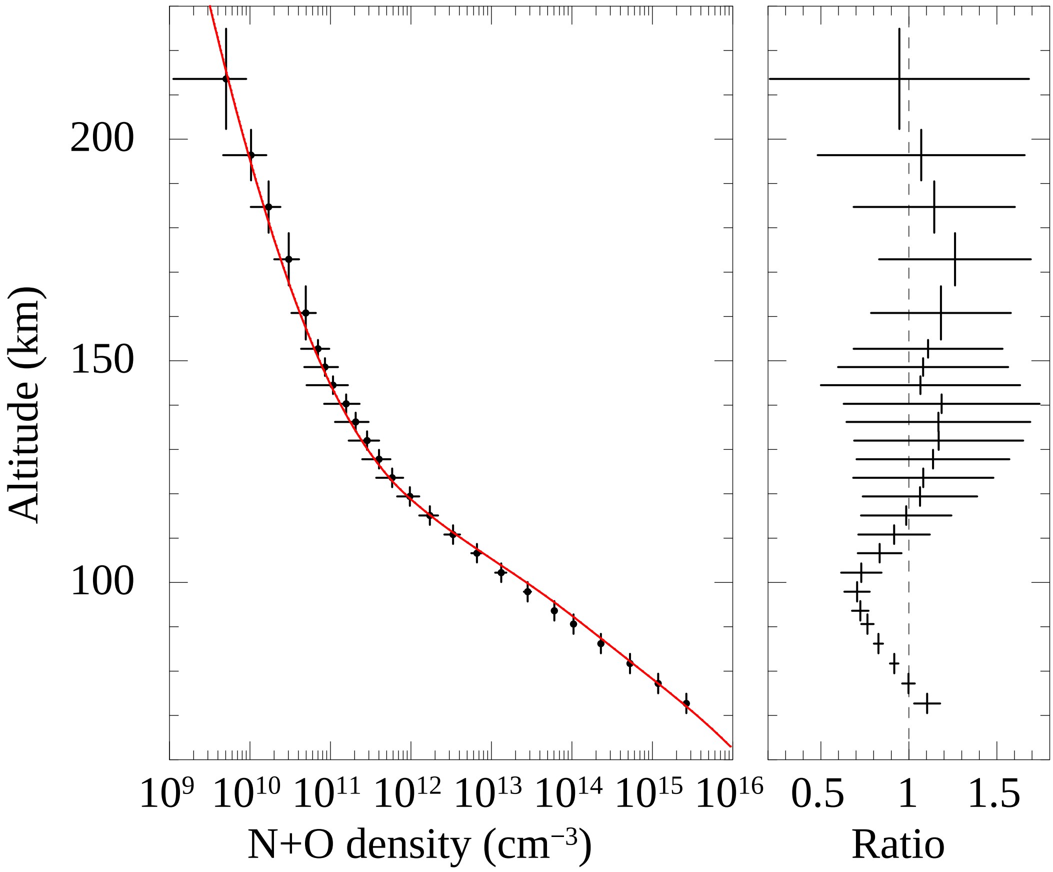

Figure 9. Left: Same as Figure 8 but the model curve in red is the mean on 2016-03-26. Right: Ratio between the data and model shown in the left panel.

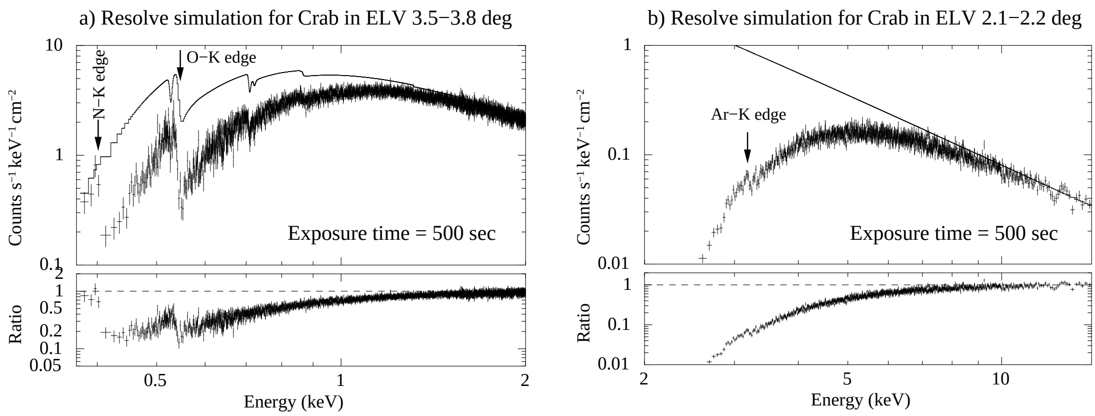

Figure 10. Crab nebula's X-ray spectra to be obtained with XRISM/Resolve, at ELV 3.5°–3.8° (left) and ELV 2.1°–2.2° (right). Lower panels show ratios between the data and the model which does not take account of the Earth's atmospheric absorption. Due to the atmospheric absorption, the K-shell edges of N, O, and Ar are clearly seen, from which we will be able to measure the chemical composition of the atmosphere.